

Article

A Study on the Effect of Graphene in Enhancing the Electrochemical Properties of SnO₂-Fe₂O₃ Anode Materials

Guanglin Zhu ¹, Bo Gao ^{1,*} , Ying Zhang ¹, Zeyuan Shi ¹, Zongbin Li ² and Ganfeng Tu ¹

¹ Key Laboratory for Ecological Metallurgy of Multimetallurgical Mineral (Ministry of Education), Northeastern University, Shenyang 110819, China

² Key Laboratory for Anisotropy and Texture of Materials (Ministry of Education), School of Materials Science and Engineering, Northeastern University, Shenyang 110819, China

* Correspondence: gaob@smm.neu.edu.cn

Abstract: To enhance the conductivity and volume expansion during the charging and discharging of transition metal oxide anode materials, rGO-SnO₂-Fe₂O₃ composite materials with different contents of rGO were prepared by the in situ hydrothermal synthesis method. The SEM morphology revealed a sphere-like fluffy structure, particles of the 0.4%rGO-10%SnO₂-Fe₂O₃ composite were smaller and more compact with a specific surface area of 223.19 m²/g, the first discharge capacity of 1423.75 mAh/g, and the specific capacity could be maintained at 687.60 mAh/g even after 100 cycles. It exhibited a good ratio performance and electrochemical reversibility, smaller charge transfer resistance, and contact resistance, which aided in lithium-ion transport. Its superior electrochemical performance was due to the addition of graphene, which made the spherical particle size distribution more uniform, effectively lowering the volume expansion during the process of charging and discharging and improving the electrochemical cycle stability of the anode materials.

Keywords: transition metal oxide; rGO; specific surface area; discharge capacity; cycle stability



Citation: Zhu, G.; Gao, B.; Zhang, Y.; Shi, Z.; Li, Z.; Tu, G. A Study on the Effect of Graphene in Enhancing the Electrochemical Properties of SnO₂-Fe₂O₃ Anode Materials. *Materials* **2022**, *15*, 7947. <https://doi.org/10.3390/ma15227947>

Academic Editor: Antonio Cardone

Received: 14 September 2022

Accepted: 27 October 2022

Published: 10 November 2022

Publisher's Note: MDPI stays neutral with regard to jurisdictional claims in published maps and institutional affiliations.



Copyright: © 2022 by the authors. Licensee MDPI, Basel, Switzerland. This article is an open access article distributed under the terms and conditions of the Creative Commons Attribution (CC BY) license (<https://creativecommons.org/licenses/by/4.0/>).

1. Introduction

The acceleration of social progress and industrialization will create an increasingly high demand for energy resources. At present, the commercial lithium-ion battery anode material is mainly graphite, which has a small theoretical specific capacity (372 mAh/g) and hence cannot meet the power supply demand of large equipment [1–3]. Therefore, the development of lithium-ion battery anode materials with high specific capacity and stable cycle performance is a relevant research area. Compared with traditional graphite anode materials, transition metal oxide materials have a higher theoretical specific capacity [4–6]. For instance, Fe₂O₃ and SnO₂ have a theoretical specific capacity of approximately 1004 and 783 mAh/g, respectively. These materials also have the advantages of low working potential, simple charging and discharging cycles, and abundant reserves, which makes them potential candidates [7–9]. However, in practical application, there are some drawbacks, such as volume expansion, low conductivity, and poor cycle stability [10–15], which might affect the battery life. Structural modification and carbon material coating treatment are the commonly adopted methods to improve its electrochemical performance [16–18].

Cui et al. [19] used a template method to prepare SnO₂@Fe₂O₃ double-shell hollow spheres. For a current density of 100 mA/g, the specific discharge capacity decreased to 464 mAh/g after 46 cycles while increased to 1043 mAh/g after 190 cycles, showcasing better electrochemical performance. Chai et al. [20] used glucose as a carbon source and ferric nitrate as an iron source to obtain anode materials by the one-step hydrothermal method followed by argon atmosphere annealing. The material possessed high crystallinity and good thermal stability. At 0.1 A/g current density, the specific capacity was 826 mAh/g after 20 cycles, and the coulomb efficiency reached 99%. Lv et al. [21] prepared carbon-coated α-Fe₂O₃ nanostructured anode materials by simple pyrolysis deposition of ferrocene

on stainless steel substrates. After 300 cycles at a current density of 500 mA/g, it could still retain a high reversible specific capacity of 1138 mAh/g.

Due to the unique structure of graphene, it can show good electrochemical performance when used as the anode material of lithium-ion batteries [22–26]. The loss of oxygen-containing functional groups increases the spacing between graphene layers, which is conducive to Li^+ embedding and removal, alleviating volume expansion [27–35]. Zhou et al. [36] prepared Fe_2O_3 /graphene nano-sheets by a simple and effective spray drying method, which showed a specific capacity of 711 mAh/g after 50 cycles of charging and discharging, and the chemical properties were quite improved. Qin et al. [37] prepared porous Fe_2O_3 /N-doped graphene (Fe_2O_3 /N-rGO) anode materials by a one-step in situ hydrothermal growth method. The porous structure and the introduction of curly GO greatly improved the electrochemical performance of the composite electrode, and the discharge-specific capacity was maintained at 1072.5 mAh/g after 100 cycles. Yang et al. [38] introduced a method for fabricating graphene-encapsulated metal oxides (GE-MO) via the co-assembly of negatively charged GO and positively charged oxide nanoparticles. The process was driven by the mutual electrostatic interaction of the oppositely charged particles, followed by chemical reduction generating GE-MO. The detection results showed that the electrochemically active Co_3O_4 nanoparticle coated with graphene (GE- Co_3O_4) exhibited a high reversible specific capacity of 1100 mAh/g during the first 10 cycles, and the reversible specific capacity could be maintained at 1000 mAh/g even after 130 cycles, showing excellent cycling performance. Therefore, it exhibited great potential as an anode material for lithium storage. Lian et al. [39] developed a gas-liquid interface synthesis method to prepare nano SnO_2 /graphene composites. The SnO_2 nanoparticles could be uniformly distributed on the graphene substrate and showed a reversible specific capacity of 1304 mAh/g at a current density of 100 mA/g. Zhou et al. [40] synthesized Sn nanoparticles/graphene composites as anode materials for lithium-ion batteries and graphene nano-sheets as a reducing agent and support layer. In the G/Sn/G layer superposition structure, the large area and elastic space were provided by graphene sheets, and the Sn nanoparticles showed excellent electrical conductivity [41–44]. The material exhibited good electrochemical performance and cyclic stability. Wang et al. [45] combined 3D hydrogels with nitrogen-containing graphene. This graphene lamellar structure had a dense microstructure and high density, and a single graphene lamellar could provide conductive pathways for electrons and more edges to enhance Li^+ embedding. Hu et al. [46] synthesized monohybrids by wrapping hollow SnO_2 nanospheres with GO. This compound exhibited excellent electrochemical performance with a high reversible specific capacity of 1107 mAh/g after 100 cycles at a current density of 0.1 A/g.

To enhance the conductivity and volume expansion in the charging and discharging cycles of transition metal oxide anode materials, this paper employed the in situ hydrothermal synthesis method to prepare rGO- SnO_2 - Fe_2O_3 composite materials. The phase composition and microstructure were determined by XRD and SEM. The charge and discharge performance, cycle performance, rate performance, and AC impedance of the materials were tested. The physical and chemical properties and internal mechanisms of the composite materials were explored.

2. Experiment

2.1. Preparation of Anode Materials

A certain amount of graphene oxide was added to deionized water and ultrasonic dispersion for 1 h, then the percentage of tin chloride and ferric chloride was dissolved. Then, sodium hydroxide solution (1 mol/L) was added during the mixing process until the solution pH reached approximately 9. After stirring for 4 h, the mixture was shifted to the high-pressure reaction kettle (Sinopharm Chemical Reagent Co., Ltd., Shenyang, China) for 4 h under 100 °C. It was further cooled to room temperature and allowed to stand for 8 h, washed, dried at 60 °C for 24 h, and lastly, vacuum roasted at 400 °C for 4 h to obtain the rGO- SnO_2 - Fe_2O_3 composite metal oxide. The Sn content was calculated as SnO_2 , the mass

percentage was fixed at 10%, and the graphene content was varied as 0.2%, 0.4%, 0.6%, and 0.8%, respectively.

2.2. Electrode Sheet Preparation

The prepared anode material was used as the active material, acetylene black was used as the conductive agent, and PVDF was used as the binder. The mass ratio was fixed as 8:1:1. N-methyl pyrrolidone (NMP) was used as the solvent to prepare the slurry. After coating, vacuum drying at 80 °C for 12 h, and stamping, the electrode sheet was ready for use.

2.3. The Battery Assembly

The electrochemical performance tests of electrode materials were executed by using the half-cell test system, the prepared electrode sheet as the anode, the lithium sheet as the counter electrode and auxiliary electrode, the polypropylene microporous membrane (Celgard-2400, Charlotte, NC, USA) as the diaphragm, and 1 mol/L LiPF₆/ethylene carbonate (EC) + dimethyl carbonate (DMC) (volume ratio was 1:1) mixture solution was used as the electrolyte. The battery was assembled according to a certain sequence of a positive shell, electrode sheet, diaphragm, lithium sheet, gasket, spring sheet, and negative shell. During the assembly process, the electrolyte was added to both sides of the diaphragm.

2.4. Characterizations

The surface morphology of the anode material was observed and analyzed by a SSX-550 tungsten filament analytical scanning electron microscope (Shimadzu Corporation, Kyoto, Japan).

A X'Pert Pro MPD diffractometer PW3040/60 manufactured by Koninklijke Philips N.V., Amsterdam, The Netherlands was used. The K α of the Cu target was the radiation source (wavelength 1.540598 Å), the working voltage was 40 kV, the sweep speed was set as 6°/min, and the sweep range was 10–90°.

The surface area tester (Micromeritics ASAP 2020) produced by Micromeritics (Pudong, China) was used to calculate the specific surface area of the sample by Brunauer–Emmett–Teller (BET) isotherm method.

2.5. Electrochemical Performance Test

A constant current charge/discharge test was carried out following the steps of static-constant current discharge-static-constant current charge-constant voltage charge. The test voltage window was set as 0.01–3 V. The charge and discharge current values were calculated from the theoretical specific capacity and the mass of the active substance.

The instrument used for the cyclic voltammetry test was the CHI660D electrochemical workstation of Shanghai Chenhua Company, Shanghai, China. The test conditions were as follows: scan rate of 0.1 mV/s, the voltage scan range of 0–3.0 V.

In the Electrochemical impedance spectroscopy test, the frequency range was 0.01 Hz–1 MHz, and the voltage vibration amplitude was 5 mV.

3. Results and Discussion

3.1. Microstructure Morphology and Specific Surface Area

Figure 1 shows the SEM of the rGO-SnO₂-Fe₂O₃ composite oxide samples with varying graphene contents, and the corresponding specific surface area is listed in Table 1. The 10%SnO₂-Fe₂O₃ composite oxide exhibited an irregular structure. After adding graphene, the rGO-10%SnO₂-Fe₂O₃ composite materials exhibited a globular fluffy structure, and the granular complex was distributed on the surface of the gossamer graphene, in between the lamellae (Figure 1). The gap between the particles could be filled with the later added conductive agent and binder. This addition, in turn, helped speed up the electron transmission, and the graphene with small resistance could inhibit the volume expansion effect during the charging and discharging process. By comparing the SEM images of rGO-SnO₂-Fe₂O₃

composites with varying graphene contents, it could be found that 0.4%rGO-10%SnO₂-Fe₂O₃ composites had the best microstructure morphology with smaller and more spherical particles, which are closely packed as well. The complex particles were evenly dispersed and tightly fixed on the curled, wrinkled surface of graphene, and the corresponding specific surface area was 223.19 m²/g. When the amount of graphene was too large, as in 0.8%rGO-10%SnO₂-Fe₂O₃, the agglomeration phenomenon was obvious, leading to a large number of sheet structures, and the specific surface area was 204.33 m²/g, which was not ideal for the transport of lithium ions during the charging and discharging process. The addition of graphene avoided the phenomenon of the anode material getting expanded or even the outer layer falling off during the charging or discharging process of lithium-ion batteries.

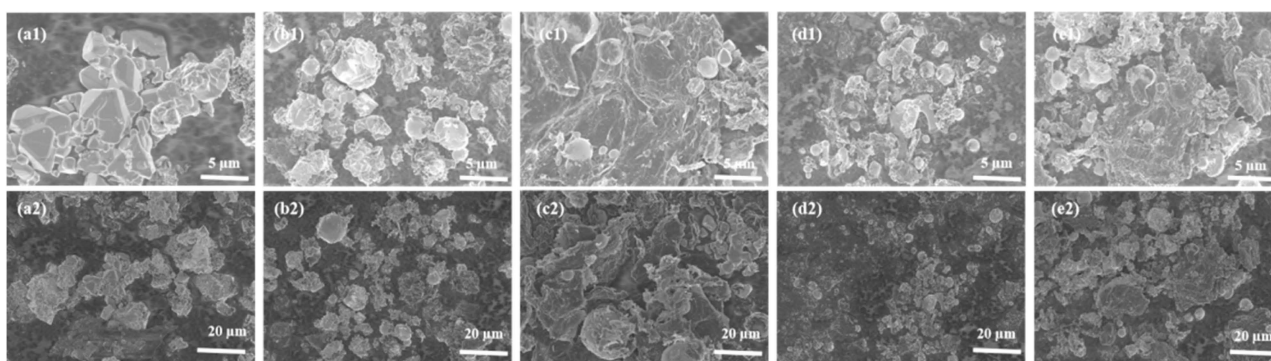


Figure 1. SEM images of rGO-SnO₂-Fe₂O₃ composites. (a1) High magnification image of 10%SnO₂-Fe₂O₃; (a2) Low magnification image of 10%SnO₂-Fe₂O₃; (b1) High magnification image of 0.2%rGO-10%SnO₂-Fe₂O₃; (b2) Low magnification image of 0.2%rGO-10%SnO₂-Fe₂O₃; (c1) High magnification image of 0.4%rGO-10%SnO₂-Fe₂O₃; (c2) Low magnification image of 0.4%rGO-10%SnO₂-Fe₂O₃; (d1) High magnification image of 0.6%rGO-10%SnO₂-Fe₂O₃; (d2) Low magnification image of 0.6%rGO-10%SnO₂-Fe₂O₃; (e1) High magnification image of 0.8%rGO-10%SnO₂-Fe₂O₃; (e2) Low magnification image of 0.8%rGO-10%SnO₂-Fe₂O₃.

Table 1. Specific surface area of rGO-SnO₂-Fe₂O₃ composite oxides.

Samples	SnO ₂ -Fe ₂ O ₃	0.2%rGO-SnO ₂ -Fe ₂ O ₃	0.4%rGO-SnO ₂ -Fe ₂ O ₃	0.6%rGO-SnO ₂ -Fe ₂ O ₃	0.8%rGO-SnO ₂ -Fe ₂ O ₃
S _{BET} (m ² /g)	145.43	183.67	223.19	216.99	204.33

3.2. Phase Composition Analysis

The XRD patterns of rGO-SnO₂-Fe₂O₃ composites with different graphene contents are shown in Figure 2. The peak patterns of rGO-SnO₂-Fe₂O₃ composite compounds with different graphene contents were similar (Figure 2). Only the characteristic diffraction peaks of SnO₂ are shown in the XRD pattern, suggesting that the main phase of rGO-SnO₂-Fe₂O₃ composites is SnO₂. There were no characteristic peaks corresponding to graphene and Fe₂O₃ in the XRD pattern, possibly because the content of graphene was low, and iron oxide might exist in an amorphous form, or enter the lattice inside of tin oxide during the recombination process to form the solid solution.

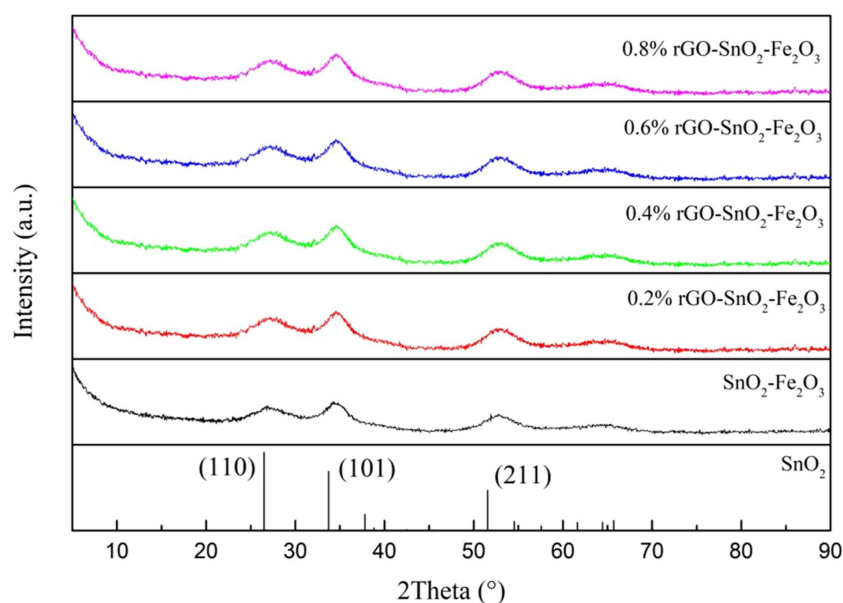


Figure 2. XRD patterns of rGO-SnO₂-Fe₂O₃ composites.

3.3. Cyclic Performance Analysis

Figure 3 shows the cycle performance curves of rGO-SnO₂-Fe₂O₃ complexes with different graphene contents at a current density of 100 mA/g. As shown in Figure 3, the first discharge-specific capacity of rGO-SnO₂-Fe₂O₃ composites increased significantly with graphene addition, indicating that the addition could improve the transport and diffusion of lithium ions, and the specific capacity of the material was improved. With graphene content increasing, capacity firstly increased and then decreased, and the capacity of 0.4%rGO-SnO₂-Fe₂O₃ reached the maximum. The specific capacity loss in the first cycle was due to the formation of solid electrolyte interface film [47,48]. It is also worth noting that the cycling performance of rGO-SnO₂-Fe₂O₃ composite was significantly improved with an increased amount of graphene compared with that of 10% SnO₂-Fe₂O₃ composite oxide. Among them, the 0.4%rGO-10%SnO₂-Fe₂O₃ anode material showed the best cycling performance, the first discharge-specific capacity was approximately 1423.75 mAh/g, and the cycle stability was at its best. The discharge-specific capacity was retained at approximately 839.76 mAh/g after 10 cycles. After 50 cycles, the discharge-specific capacity could be kept close to 744.05 mAh/g, which was mainly due to the more uniform distribution of spherical particles in the microstructure of 0.4%rGO-10%SnO₂-Fe₂O₃. When the graphene content was increased to 0.8%, the cycling performance of 0.8%rGO-10%SnO₂-Fe₂O₃ decreased significantly, which might be due to the high agglomeration tendency of material particles caused by the excessive amount of graphene.

To explore the cycle life and stability of the 0.4%rGO-10%SnO₂-Fe₂O₃ anode material, 100 cycles of constant current charge and discharge, and constant current at different rates are shown in Figure 4. According to the test results in Figure 4a, the discharge specific capacity of the 0.4%rGO-10%SnO₂-Fe₂O₃ anode material was maintained at approximately 687.60 mAh/g even after 100 cycles. In subsequent tests, although the specific capacity decreased to a small extent, the change was very gentle, indicating that the material had relatively stable cycling performance. It could be seen from Figure 4b, that after different rate tests, the specific capacity of the 0.4%rGO-10%SnO₂-Fe₂O₃ anode material decreased with an increase in the rate, but the overall decline rate was relatively slow. When the rate was 0.2 C, the discharge capacity was 763.82 mAh/g; however, at a 2 C rate, the specific capacity was 556.77 mAh/g. The specific capacity was 556.77 mAh/g when the rate was restored to 0.2 C, while the specific discharge capacity was not reduced but increased to 651 mAh/g. This result indicates that the overall performance of the material was improved to a certain extent due to the mutual synergistic effect of the combination of

different components. Moreover, after a period of charging and discharging, the infiltration of the electrolyte and the volume change led to a more stable structure of the anode material, and thus its discharge-specific capacity was improved.

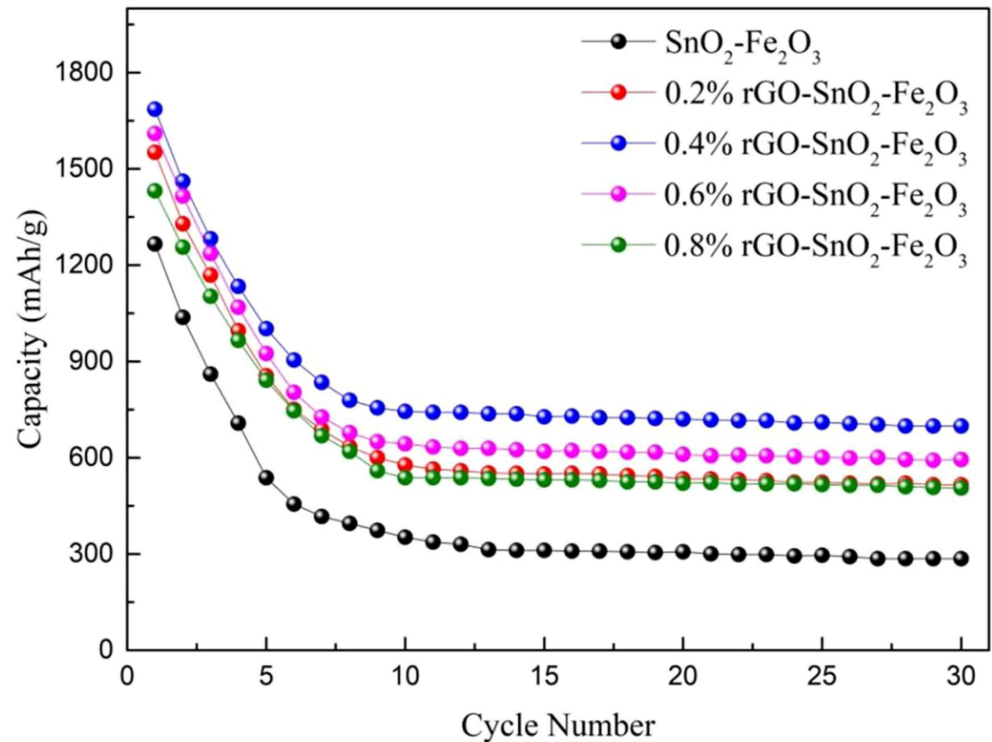


Figure 3. Cyclic performance of rGO-SnO₂-Fe₂O₃ composites.

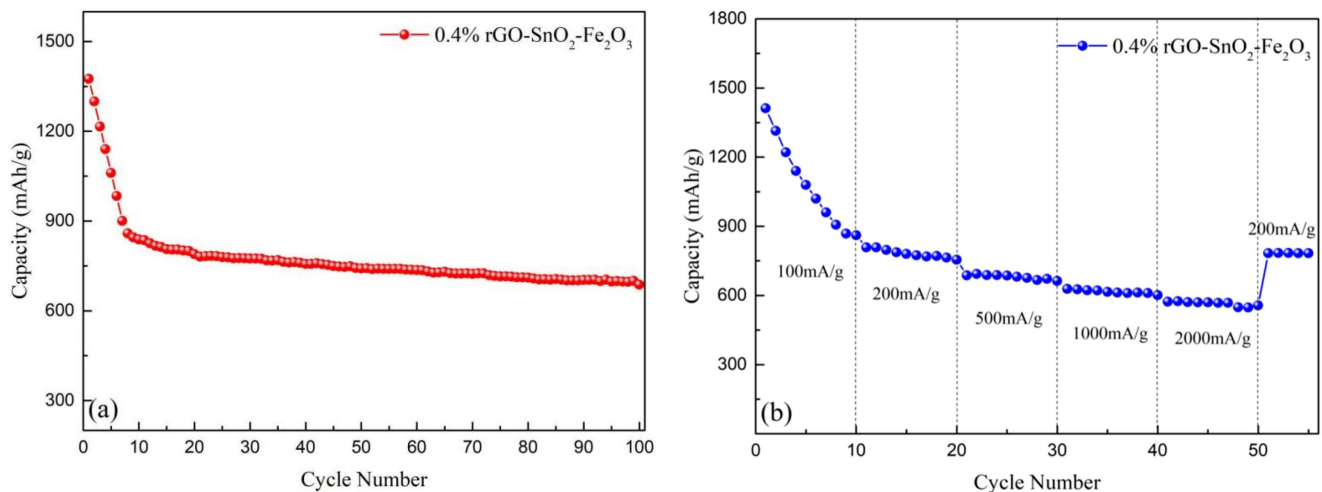


Figure 4. Cyclic performance diagrams of the 0.4%rGO-10SnO₂-Fe₂O₃ anode material. (a) A total of 100 discharge cycles; (b) Magnification curve.

3.4. Charge and Discharge Curve Analysis

The first three charge and discharge tests of 10%SnO₂-Fe₂O₃ and 0.4%rGO-10%SnO₂-Fe₂O₃ anode materials were carried out, as shown in Figure 5. According to Figure 5a, in the first discharge process of the 10%SnO₂-Fe₂O₃ sample, there was a flat and long discharge platform at approximately 0.8 V, and a relatively slow charging voltage platform at 1.5–1.8 V appeared in the first charging curve. Similarly, from Figure 5b, it can be seen that during the first discharge process of the 0.4%rGO-10%SnO₂-Fe₂O₃ sample, there was a short platform approximately 2.0 V, a flat long platform approximately 0.8–0.9 V, and a slow

charging platform between 1.0 and 1.5 V in the first charging curve. The first discharge exhibited the largest specific capacity, and the second turn had the smallest specific capacity loss. The second and third charge and discharge curves showed a gentle variation trend, higher coincidence, and better electrochemical reversibility, which can be attributed to the fact that the addition of graphene made the distribution of the spherical particles more uniform, leading to an alleviated volume expansion effect during the process of charge and discharge thereby improving the electrochemical stability of anode materials.

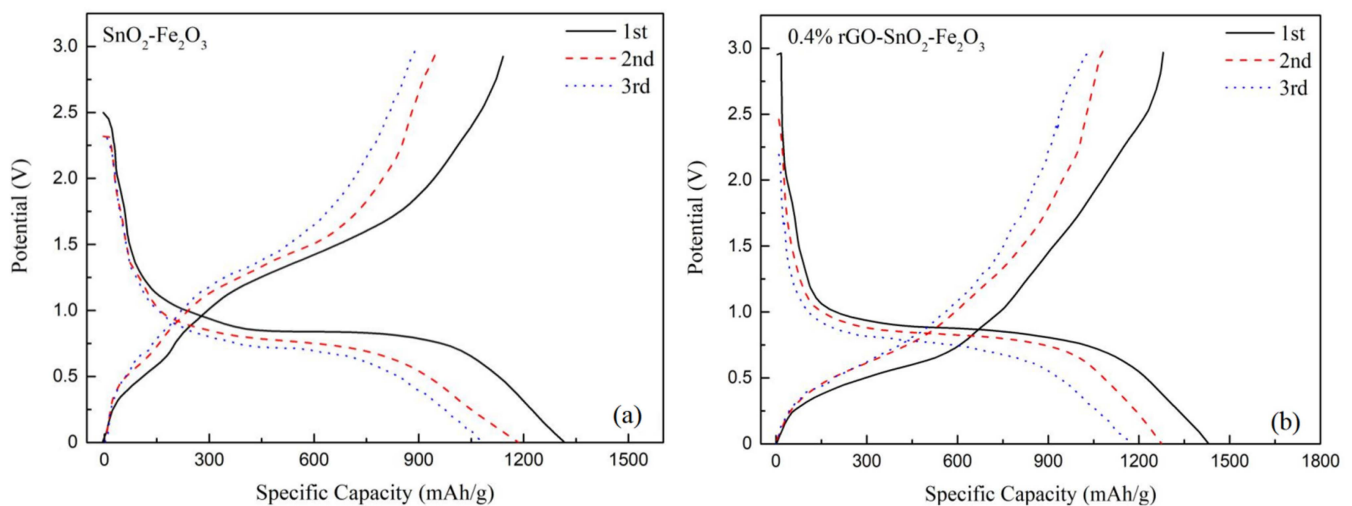


Figure 5. The first three-time capacity-voltage curves. (a) 10%SnO₂-Fe₂O₃; (b) 0.4%rGO-10%SnO₂-Fe₂O₃.

3.5. Cyclic Voltammetry Curve Analysis

Cyclic voltametric curves of 10%SnO₂-Fe₂O₃ and 0.4%rGO-10%SnO₂-Fe₂O₃ are shown in Figure 6. As can be seen from Figure 6a, the reduction peak of 10%SnO₂-Fe₂O₃ in the first turn appeared near 0.78 V, which corresponds to the conversion of Fe³⁺ to Fe⁰. In addition, there was a smaller reduction peak located at 1.3 V, which was assigned to the reduction of Sn⁴⁺ to Sn²⁺. However, the peak was of significantly low intensity. The oxidation peak in the first cycle appeared at 1.7–2.2 V, which corresponds to the transformation of Fe⁰ to Fe³⁺ and Sn²⁺ to Sn⁴⁺. In the following two cycles, the intensity of the oxidation peak decreased slightly, and the overlap of cyclic voltammetry curves was good. Figure 6b shows the charging and discharging cyclic voltammetry curves of 0.4%rGO-10%SnO₂-Fe₂O₃ for the first three times. The reduction peak of 0.4%rGO-10%SnO₂-Fe₂O₃ in the first turn appeared near 0.7 V, which corresponded to the conversion of Fe³⁺ to Fe⁰. In addition, there was a smaller reduction peak located at 1.3 V attributable to Sn⁴⁺ to Sn²⁺ conversion [49–51]. In the following two turns, the position of the reduction peak from Fe³⁺ to Fe⁰ did not move, but the peak intensity was significantly weakened due to the formation of solid electrolyte interface film (SEI film) [52,53], and the reduction peak from Sn⁴⁺ to Sn²⁺ disappeared. The oxidation peaks of the first cycle appeared at 1.7 V and 2.0 V, corresponding to the transformation of Fe⁰ to Fe³⁺ and Sn²⁺ to Sn⁴⁺. The cyclic voltammetry curves overlapped well, suggesting higher reversibility and better stability.

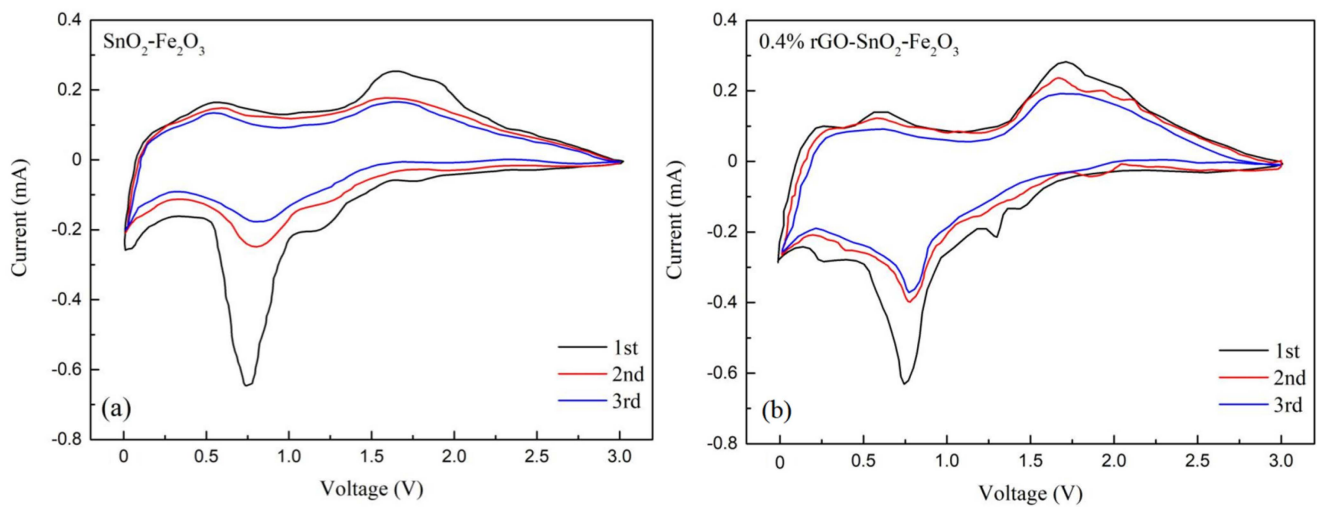


Figure 6. Cyclic voltametric curve. (a) 10%SnO₂-Fe₂O₃; (b) 0.4% rGO-10%SnO₂-Fe₂O₃.

3.6. AC Impedance Analysis

The AC impedance spectra of rGO-SnO₂-Fe₂O₃ composites with different graphene contents are shown in Figure 7. The AC impedance spectra of all samples consisted of a semicircle in the high-frequency region and a straight line in the low-frequency region. The radius of the semicircle represented the electron transfer resistance at the electrode/solution interface, which was also the charge transfer impedance at the electrode interface and corresponded to the contact resistance of the anode material [54]. The slope of the line represented the mobility of lithium ions inside the electrode, namely the Warburg impedance, which could be related to the charge transfer resistance [55–58]. Figure 7 showed that the resistance value of composite material increases in the order: 0.4%rGO-10%SnO₂-Fe₂O₃, 0.6%rGO-10%SnO₂-Fe₂O₃, 0.8%rGO-10%SnO₂-Fe₂O₃, 0.2%rGO-10%SnO₂-Fe₂O₃ and 10%SnO₂-Fe₂O₃. After graphene addition, the resistance of the material decreased, which was closely related to the effect of graphene on the microstructure. Among them, when the graphene content was 0.4%, the 0.4%rGO-10%SnO₂-Fe₂O₃ anode material possessed the smallest semi-circuit radius, indicating that it had the smallest contact resistance and charge transfer resistance, which was conducive to the transport of lithium ions and was consistent with the cycling performance results. With the amount of graphene increasing, as in 0.8%rGO-10%SnO₂-Fe₂O₃, the charge transfer resistance was increased due to the agglomeration phenomenon and lower specific surface area.

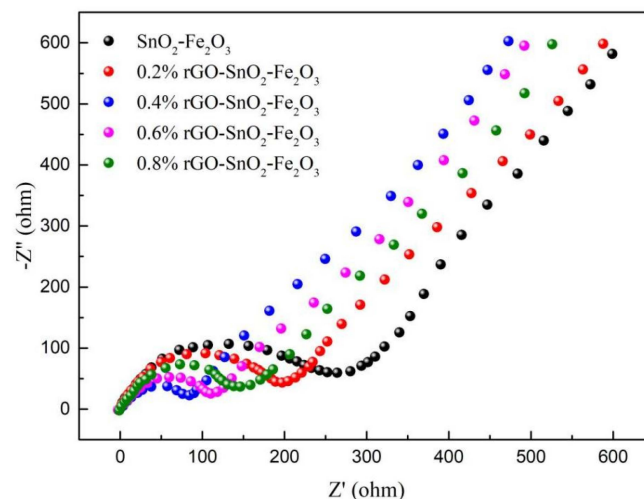


Figure 7. AC impedance diagrams of rGO-SnO₂-Fe₂O₃ composites.

4. Conclusions

In this paper, rGO-SnO₂-Fe₂O₃ anode materials were prepared by using SnO₂-Fe₂O₃ as the matrix and adding graphene oxide in varying contents. The structural characterization and electrochemical performance of the above materials were investigated, and the following conclusions were drawn: (1) The phase structure of the rGO-SnO₂-Fe₂O₃ composite was SnO₂, and the morphology was a globular fluffy structure. The granular complex was distributed on the surface and between the lamellae of the bubble graphene. The morphology of 0.4%rGO-10%SnO₂-Fe₂O₃ composite was the best, and the spherical particles were smaller and more in numbers. The spherical particles were more closely packed, and the specific surface area was 223.19 m²/g. (2) The cycle performance of the 0.4%rGO-10%SnO₂-Fe₂O₃ anode material was the best, the first discharge-specific capacity was 1423.75 mAh/g, and after 100 cycles, the capacity was maintained at approximately 687.60 mAh/g. The results of different rate tests showed that the specific capacity of the 0.4%rGO-10%SnO₂-Fe₂O₃ anode material decreased with an increase in the rate, but the overall rate of decline was relatively slow. (3) 0.4%rGO-10%SnO₂-Fe₂O₃ exhibited better electrochemical reversibility, smaller contact resistance, and charge transfer resistance. All these characteristics were beneficial to the transport of lithium ions and were consistent with the cycling performance results. (4) The excellent electrochemical performance of 0.4%rGO-10%SnO₂-Fe₂O₃ can be attributed to the addition of graphene, which made the size distribution of spherical particles more uniform, effectively alleviating the volume expansion phenomenon during the process of charging and discharging. This has further enhanced the electrochemical cycle stability of anode materials. It can be seen from the experimental results that the addition of graphene can improve the specific capacity and cycle stability. However, it has no significant effect on the capacity attenuation in the first lap, which will be paid more attention in the later research.

Author Contributions: Conceptualization, G.Z. and B.G.; validation, G.Z.; methodology, G.Z.; formal analysis, G.Z. and Y.Z.; investigation, G.Z., Y.Z., Z.L. and Z.S.; resources, Y.Z., Z.L. and Z.S.; writing—original draft preparation, G.Z.; writing—review and editing, B.G. and G.T.; supervision, G.T.; project administration, B.G. All authors have read and agreed to the published version of the manuscript.

Funding: This research was funded by the National Natural Science Foundation of China, grant number 51671052; the Fundamental Research Funds for the Central Universities, grant number N182502042; the Liao Ning Revitalization Talents Program, grant number XLYC1902105; and the Shenyang Science and Technology Plan, grant number 20-203-5-39.

Institutional Review Board Statement: Not applicable.

Informed Consent Statement: Not applicable.

Data Availability Statement: All data generated and analyzed during this study are included in this article.

Conflicts of Interest: The authors declare no conflict of interest.

References

1. Zardkhoshoui, A.M.; Bahareh, A.; Davarani, S.S.H. Fabrication of hollow MnFe₂O₄ nanocubes assembled by CoS₂ nanosheets for hybrid supercapacitors. *Chem. Eng. J.* **2022**, *435*, 135170. [[CrossRef](#)]
2. Zardkhoshoui, A.M.; Bahareh, A.; Davarani, S.S.H. α -MnS@Co₃S₄ hollow nanospheres assembled from nanosheets for hybrid supercapacitors. *Chem. Eng. J.* **2021**, *422*, 129953. [[CrossRef](#)]
3. Zardkhoshoui, A.M.; Davarani, S.S.H. Construction of complex copper-cobalt selenide hollow structures as an attractive battery-type electrode material for hybrid supercapacitors. *Chem. Eng. J.* **2020**, *402*, 126241. [[CrossRef](#)]
4. Chen, Y.; Liang, J.; Tian, Q.; Zhang, W.; Sui, Z. Facile construction of clustered Fe₂O₃/TiO₂ composite for improved lithium storage performance. *Synth. Met.* **2020**, *263*, 116353. [[CrossRef](#)]
5. Zhang, Z.; Liang, J.; Zhang, X.; Yang, W.; Dong, X.; Jung, Y. Dominant pseudocapacitive lithium storage in the carbon-coated ferric oxide nanoparticles (Fe₂O₃@C) towards anode materials for lithium-ion batteries. *Int. J. Hydr. Energy* **2020**, *45*, 8186–8197. [[CrossRef](#)]

6. Zuniga, L.; Gonzalez, G.; Orrostieta Chavez, R.; Myers, J.C.; Lodge, T.P.; Alcoutlabi, M. Centrifugally spun α -Fe₂O₃/TiO₂/carbon composite fibers as anode materials for lithium-ion batteries. *Appl. Sci.* **2019**, *9*, 403211–403217. [[CrossRef](#)]
7. Zardkhoshoui, A.M.; Bahareh, A.; Davarani, S.S.H. A high-energy-density supercapacitor with multi-shelled nickel-manganese selenide hollow spheres as cathode and double-shell nickel-iron selenide hollow spheres as anode electrodes. *Nanoscale* **2021**, *13*, 2931–2945. [[CrossRef](#)]
8. Zardkhoshoui, A.M.; Davarani, S.S.H. Boosting the energy density of supercapacitors by encapsulating a multi-shelled zinc-cobalt-selenide hollow nanosphere cathode and a yolk-double shell cobalt-iron-selenide hollow nanosphere anode in a graphene network. *Nanoscale* **2020**, *12*, 12476–12489. [[CrossRef](#)]
9. Zardkhoshoui, A.M.; Davarani, S.S.H.; Ashtiani, M.M.; Sarparast, M. Designing an asymmetric device based on graphene wrapped yolk-double shell NiGa₂S₄ hollow microspheres and graphene wrapped FeS₂-FeSe₂ core-shell cratered spheres with outstanding energy density. *J. Mater. Chem. A* **2019**, *7*, 10282–10292. [[CrossRef](#)]
10. Asakura, D.; Nanba, Y.; Okubo, M.; Niwa, H.; Kiuchi, H.; Miyawaki, J.; Oshima, M.; Hosono, E.; Harada, Y. Operando soft X-ray emission spectroscopy of the Fe₂O₃ anode to observe the conversion reaction. *Phys. Chem. Chem. Phys.* **2019**, *21*, 26351–26357. [[CrossRef](#)]
11. Chen, J.S.; Zhu, T.; Yang, X.H.; Yang, H.G.; Lou, X.W. Top-down fabrication of α -Fe₂O₃ single-crystal nanodiscs and microparticles with tunable porosity for largely improved lithium storage properties. *J. Am. Chem. Soc.* **2010**, *132*, 13162–13164. [[CrossRef](#)]
12. Reddy, M.V.; Yu, T.; Sow, C.H.; Shen, Z.X.; Lim, C.T.; Subba Rao, G.V.; Chowdari, B.V.R. α -Fe₂O₃ nanoflakes as an anode material for Li-ion batteries. *Adv. Funct. Mater.* **2007**, *17*, 2792–2799. [[CrossRef](#)]
13. Zhang, B.; Huang, Z.D.; Oh, S.W.; Kim, J.K. Improved rate capability of carbon coated Li_{3.9}Sn_{0.1}Ti₅O₁₂ porous electrodes for Li-ion batteries. *J. Power Sources* **2011**, *196*, 10692–10697. [[CrossRef](#)]
14. Wu, M.S.; Ou, Y.H.; Lin, Y.P. Iron oxide nanosheets and nanoparticles synthesized by a facile single-step coprecipitation method for lithium-ion batteries. *J. Electrochem. Soc.* **2011**, *158*, 231–236. [[CrossRef](#)]
15. Tian, L.L.; Zhang, M.J.; Wu, C.; Wei, Y.; Zheng, J.X.; Lin, L.P.; Lu, J.; Amine, K.; Zhuang, Q.C.; Pan, F. γ -Fe₂O₃ nanocrystalline microspheres with hybrid behavior of battery-supercapacitor for superior lithium storage. *ACS Appl. Mater. Interfaces* **2015**, *7*, 26284–26290. [[CrossRef](#)]
16. Bahareh, A.; Zardkhoshoui, A.M.; Davarani, S.S.H. An advanced hybrid supercapacitor constructed from rugby-ball-like NiCo₂Se₄ yolk-shell nanostructures. *Mater. Chem. Front.* **2021**, *5*, 4725–4738.
17. Zardkhoshoui, A.M.; Davarani, S.S.H. Formation of graphene-wrapped multi-shelled NiGa₂O₄ hollow spheres and graphene-wrapped yolk-shell NiFe₂O₄ hollow spheres derived from metal-organic frameworks for high-performance hybrid supercapacitors. *Nanoscale* **2020**, *12*, 1643–1656. [[CrossRef](#)]
18. Pan, Y.; Yin, L.; Li, M. Submicron-sized α -Fe₂O₃ single crystals as anodes for high-performance lithium-ion batteries. *Ceram. Int.* **2019**, *45*, 12072–12079. [[CrossRef](#)]
19. Cui, Z.; Sun, M.; Liu, H.; Li, S.; Zhang, Q.; Yang, C.; Liu, G.; Zhong, J.; Wang, Y. Double-shell SnO₂@Fe₂O₃ hollow spheres as a high-performance anode material for lithium-ion batteries. *CrystEngComm* **2020**, *22*, 1197–1208. [[CrossRef](#)]
20. Chai, X.; Shi, C.; Liu, E.; Li, J.; Zhao, N.; He, C. Carbon-coated Fe₂O₃ nanocrystals with enhanced lithium storage capability. *Appl. Surf. Sci.* **2015**, *347*, 178–185. [[CrossRef](#)]
21. Lv, X.; Deng, J.; Wang, J.; Zhong, J.; Sun, X. Carbon-coated α -Fe₂O₃ nanostructures for efficient anode of Li-ion battery. *J. Mater. Chem. A* **2015**, *3*, 5183–5188. [[CrossRef](#)]
22. Zardkhoshoui, A.M.; Davarani, S.S.H.; Ashtiani, M.M.; Sarparast, M. High-Performance Energy Storage Device Based on Triple-Shelled Cobalt Gallium Oxide Hollow Spheres and Graphene Wrapped Copper Iron Disulfide Porous Spheres. *ACS Sustain. Chem. Eng.* **2019**, *7*, 7908–7917. [[CrossRef](#)]
23. Zardkhoshoui, A.M.; Ashtiani, M.M.; Sarparast, M.; Davarani, S.S.H. Enhanced the energy density of supercapacitors via rose-like nanoporous ZnGa₂S₄ hollow spheres cathode and yolk-shell FeP hollow spheres Anode. *J. Power Sources* **2020**, *450*, 227691. [[CrossRef](#)]
24. Bahareh, A.; Zardkhoshoui, A.M.; Davarani, S.S.H. Engineering of hierarchical NiCoSe₂@NiMn-LDH core-shell nanostructures as a high-performance positive electrode material for hybrid supercapacitors. *Sustain. Energy Fuels* **2020**, *4*, 5144–5155.
25. Prekodravac, J.R.; Kepić, D.P.; Colmenares, J.C.; Giannakoudakis, D.A.; Jovanović, S.P. A comprehensive review on selected graphene synthesis methods: From electrochemical exfoliation through rapid thermal annealing towards biomass pyrolysis. *J. Mater. Chem. C* **2021**, *9*, 6722–6748. [[CrossRef](#)]
26. Kamedulski, P.; Lukaszewicz, J.P.; Witczak, L.; Szroeder, P.; Ziolkowski, P. The Importance of Structural Factors for the Electrochemical Performance of Graphene/Carbon Nanotube/Melamine Powders towards the Catalytic Activity of Oxygen Reduction Reaction. *Materials* **2021**, *14*, 2448. [[CrossRef](#)]
27. Lee, C.; Wei, X.; Kysar, J.W.; Hone, J. Measurement of the elastic properties and intrinsic strength of monolayer graphene. *Science* **2008**, *321*, 385–388. [[CrossRef](#)]
28. Hu, H.; Zhao, Z.; Wan, W.; Gogotsi, Y.; Qiu, J. Ultralight and highly compressible graphene aerogels. *Adv. Mater.* **2013**, *25*, 2219–2223. [[CrossRef](#)]
29. Zardkhoshoui, A.M.; Davarani, S.S.H. A rational design of nanoporous Cu-Co-Ni-P nanotube arrays and CoFe₂Se₄ nanosheet arrays for flexible solid-state asymmetric devices. *Dalton Trans.* **2020**, *49*, 10028–10041. [[CrossRef](#)]

30. Zardkhouhoui, A.M.; Davarani, S.S.H. Ultra-high energy density supercapacitors based on metal-organic framework derived yolk-shell Cu-Co-P hollow nanospheres and CuFeS₂ nanosheet arrays. *Dalton Trans.* **2020**, *49*, 3353–3364. [[CrossRef](#)]
31. Zhen, Y.X.; Arbizzani, C.; Ortolani, L.; Morandi, V.; Bellani, V.; Giambastiani, G. High yield production of graphene-Fe₂O₃ nano-composites via electrochemical intercalation of nitromethane and iron chloride, and their application in lithium storage. *FlatChem* **2017**, *3*, 8–15.
32. Zardkhouhoui, A.M.; Davarani, S.S.H.; Asgharinezhad, A.A. Designing graphene-wrapped NiCo₂Se₄ microspheres with petal-like FeS₂ toward flexible asymmetric all-solid-state supercapacitors. *Dalton Trans.* **2019**, *48*, 4274–4282. [[CrossRef](#)]
33. Dreyer, D.R.; Ruoff, R.S.; Bielawski, C.W. From conception to realization: An historical account of graphene and some perspectives for its future. *Angew. Chem. Int. Ed.* **2010**, *49*, 9336–9344. [[CrossRef](#)]
34. Cai, D.; Li, D.; Wang, S.; Zhu, X.; Yang, W.; Zhang, S.; Wang, H. High rate capability of TiO₂/nitrogen-doped graphene nanocomposite as an anode material for lithium-ion batteries. *J. Alloys Comp.* **2013**, *561*, 54–58. [[CrossRef](#)]
35. Heenen, H.H.; Shin, H.; Kastlunger, G.; Overa, S.; Gauthier, J.A.; Jiao, F.; Chan, K. The mechanism for acetate formation in electrochemical CO(2) reduction on Cu: Selectivity with potential, pH, and nanostructuring. *Energy Environ. Sci.* **2022**, *15*, 3978–3990. [[CrossRef](#)]
36. Zhou, G.-W.; Wang, J.; Gao, P.; Yang, X.; He, Y.-S.; Liao, X.-Z.; Yang, J.; Ma, Z.-F. Facile spray drying route for the three-dimensional graphene-encapsulated Fe₂O₃ nanoparticles for lithium ion battery anodes. *Ind. Eng. Chem. Res.* **2013**, *52*, 1197–1204. [[CrossRef](#)]
37. Qin, G.; Ding, L.; Zeng, M.; Zhang, K.; Zhang, Y.; Bai, Y.; Wen, J.; Li, J. Mesoporous Fe₂O₃/N-doped graphene composite as an anode material for lithium ion batteries with greatly enhanced electrochemical performance. *J. Electroanal. Chem.* **2020**, *866*, 114176. [[CrossRef](#)]
38. Yang, S.; Feng, X.; Ivanovici, S.; Müllen, K. Fabrication of graphene-encapsulated oxide nanoparticles: Towards high-performance anode materials for lithium storage. *Angew. Chem. Int. Ed.* **2010**, *49*, 8408–8411. [[CrossRef](#)]
39. Lian, P.; Zhu, X.; Liang, S.; Li, Z.; Yang, W.; Wang, H. High reversible capacity of SnO₂/graphene nanocomposite as an anodematerial for lithium-ion batteries. *Electrochim. Acta* **2011**, *56*, 4532–4539. [[CrossRef](#)]
40. Zhou, X.; Zou, Y.; Yang, J. Periodic structures of Sn self-inserted between graphene interlayers as anodes for Li-ion battery. *J. Power Sources* **2014**, *253*, 287–293. [[CrossRef](#)]
41. Cao, J.; Zhang, D.-D.; Chanajaree, R.; Yue, Y.-L.; Zeng, Z.-Y.; Zhang, X.-Y.; Qin, J.-Q. Stabilizing zinc anode via a chelation and desolvation electrolyte additive. *Adv. Powder Mater.* **2022**, *1*, 100007. [[CrossRef](#)]
42. Bahareh, A.; Zardkhouhoui, A.M.; Davarani, S.S.H. Metal-organic-framework derived hollow manganese nickel selenide spheres confined with nanosheets on nickel foam for hybrid supercapacitors. *Dalton Trans.* **2021**, *50*, 8372–8384.
43. Zhang, D.-D.; Cao, J.; Zhang, X.-Y.; Insin, N.; Liu, R.-P.; Qin, J.-Q. NiMn Layered Double Hydroxide Nanosheets In-situ Anchored on Ti₃C₂ MXene via Chemical Bonds for Superior Supercapacitors. *ACS Appl. Energy Mater.* **2020**, *3*, 5949–5964. [[CrossRef](#)]
44. Zhang, D.-D.; Cao, J.; Zhang, X.-Y.; Insin, N.; Wang, S.-M.; Zhao, Y.-S.; Qin, J.-Q. NiMn-Layered Double Hydroxides Chemically Anchored on Ti₃C₂ MXene for Superior Lithium Ion Storage. *ACS Appl. Energy Mater.* **2020**, *3*, 11119–11130. [[CrossRef](#)]
45. Wang, X.; Lv, L.; Cheng, Z.; Gao, J.; Dong, L.; Hu, C.; Qu, L. High-Density Monolith of N-Doped Holey Graphene for Ultrahigh Volumetric Capacity of Li-Ion Batteries. *Adv. Energy Mater.* **2016**, *6*, 1502100–1502106. [[CrossRef](#)]
46. Hu, X.; Zeng, G.; Chen, J.; Lu, C.; Wen, Z. 3D graphene network encapsulating SnO₂ hollow spheres as a high-performance anode material for lithium-ion batteries. *J. Mater. Chem. A* **2017**, *5*, 4535–4542. [[CrossRef](#)]
47. Li, Z.; Mao, Y.; Tian, Q.; Zhang, W.; Yang, L. Extremely facile preparation of high-performance Fe₂O₃ anode for lithium-ion batteries. *J. Alloys Comp.* **2019**, *784*, 125–133. [[CrossRef](#)]
48. Yang, L.; Wu, Y.; Wu, Y.; Younas, W.; Jia, J.; Cao, C. Hierarchical flower-like Fe₂O₃ mesoporous nanosheets with superior electrochemical lithium storage performance. *J. Energy Storage* **2019**, *23*, 363–370. [[CrossRef](#)]
49. Amiri, M.; Zardkhouhoui, A.M.; Davarani, S.S.H.; Maghsoudi, M.; Altafi, M.K. A high-performance hybrid supercapacitor by encapsulating binder-less FeCoSe₂ nanosheets@NiCoSe₂ nanoflowers in a graphene network. *Sustain. Energy Fuels* **2022**, *6*, 3626–3642. [[CrossRef](#)]
50. Cao, J.; Zhang, D.-D.; Yue, Y.-L.; Chanajaree, R.; Wang, S.-M.; Han, J.-T.; Zhang, X.-Y.; Qin, J.-Q.; Huang, Y.-H. Regulating solvation structure to stabilize zinc anode by fastening the free water molecules with an inorganic colloidal electrolyte. *Nano Energy* **2022**, *93*, 106839. [[CrossRef](#)]
51. Cao, S.-J.; Xue, Z.; Yang, C.-W.; Qin, J.-Q.; Zhang, L.; Yu, P.-F.; Wang, S.-M.; Zhao, Y.-S.; Zhang, X.-Y.; Liu, R.-P. Insights into the Li⁺ storage mechanism of TiC@C-TiO₂ core-shell nanostructures as high performance anodes. *Nano Energy* **2018**, *50*, 25–34. [[CrossRef](#)]
52. Li, B.; Gu, P.; Zhang, G.; Lu, Y.; Huang, K.; Xue, H.; Pang, H. Ultrathin Nanosheet Assembled Sn_{0.91}Co_{0.19}S₂ Nanocages with Exposed (100) Facets for High-Performance Lithium-Ion Batteries. *Small* **2018**, *14*, 725–734.
53. Poizot, P.; Laruelle, S.; Grugeon, S.; Dupont, L.; Tarascon, J.M. Nano-sized transition-metal oxides as negative-electrode materials for lithium-ion batteries. *Nature* **2000**, *407*, 496–499. [[CrossRef](#)]
54. Li, C.-Y.; Qin, J.-Q.; Sawangphruk, M.; Zhang, X.-Y.; Liu, R.-P. Rational design and synthesis of SiC/TiC@SiO_x/TiO₂ porous core-shell nanostructure with excellent Li-ion storage performance. *Chem. Commun.* **2018**, *54*, 12622–12625. [[CrossRef](#)]
55. Tomasetti, C.; Vogelstein, B. Variation in cancer risk among tissues can be explained by the number of stem cell. *Science* **2015**, *347*, 78–81. [[CrossRef](#)]
56. Zhang, J.; Yu, A. Nanostructured transition metal oxides as advanced anodes for lithium-ion batteries. *Sci. Bull.* **2015**, *60*, 823–838. [[CrossRef](#)]

57. Zhou, W.; Cheng, C.; Liu, J.; Tay, Y.Y.; Jiang, J.; Jia, X.; Zhang, J.; Gong, H.; Hng, H.H.; Yu, T. Epitaxial growth of branched α -Fe₂O₃/SnO₂ nano-heterostructures with improved lithium-ion battery performance. *Adv. Funct. Mater.* **2011**, *21*, 2439–2445. [[CrossRef](#)]
58. Yuan, S.; Zhou, Z.; Li, G. Structural evolution from mesoporous α -Fe₂O₃ to Fe₃O₄@C and γ -Fe₂O₃ nanospheres and their lithium storage performances. *CrystEngComm* **2011**, *13*, 4709–4713. [[CrossRef](#)]